Point defects in p-type transparent conductive $CuMO_2$ (M = Al, Ga, In) from first principles

Tomoya Gake, Yu Kumagai, Akira Takahashi, and Fumiyasu Oba*
Laboratory for Materials and Structures, Institute of Innovative Research, Tokyo Institute of Technology, Yokohama 226-8503, Japan

(Received 19 July 2021; revised 16 September 2021; accepted 23 September 2021; published 8 October 2021)

We investigate the native point defects in delafossite $CuMO_2$ (M = Al, Ga, In) using first-principles calculations based on the Heyd-Scuseria-Ernzerhof (HSE06) hybrid functional approach. The Cu vacancies in all the systems show low formation energies and form relatively shallow acceptor levels, which would contribute mainly to the p-type conductivity. The hole compensation by the donor-type native defects does not essentially limit the p-type doping in all of $CuMO_2$ under controlled growth conditions. In contrast, the acceptor-type native defects, especially the Cu vacancies, show low or even negative formation energies at high Fermi level positions in $CuAlO_2$ and $CuGaO_2$, thereby compensating carrier electrons to limit the n-type doping. The neutral Cu vacancy forms an in-gap state with hole localization to the neighboring Cu atoms in each of $CuMO_2$, whereas the neutral Cu-on-Al antisite in $CuAlO_2$ and the Cu-on-Ga antisite in $CuGaO_2$ form in-gap states with hole localization to themselves. In the framework of the HSE06 hybrid functional, the generalized Koopmans' theorem is almost satisfied for the Cu-on-Al and Cu-on-Ga antisites, but not for the Cu vacancies in all of $CuMO_2$. However, the absolute positions of the acceptor levels of the Cu vacancies are almost constant regardless of the convex/concave behavior of the hybrid functional controlled by the Fock-exchange parameter, suggesting that the determination of the valence band maximum is mostly relevant to accurate prediction of the acceptor level position. The n-type doping limits, namely the upper limits of the Fermi level in thermodynamic equilibrium, determined by the spontaneous formation of the Cu vacancies, are almost common to all of $CuMO_2$ in the band alignment with respect to the vacuum level. In contrast, the conduction band minimum significantly depends on the system, which suggests, along with the Fermi level restriction by the Cu-vacancy formation, that strong compensation of carrier electrons is avoidable only in $CuInO_2$. This finding indicates that the position of the conduction band minimum is an important indicator for discussing and designing n-type doping of $CuMO_2$ as proposed previously.

DOI: 10.1103/PhysRevMaterials.5.104602

I. INTRODUCTION

Transparent conductive oxides (TCOs) are indispensable materials for transparent electrodes in displays, photovoltaic cells, and so on [1]. The most prototypical TCOs are electron-doped In_2O_3 [2], SnO_2 [3–5], and ZnO [6,7], which are known to exhibit high n-type conductivity. The conduction bands of these oxides are mainly composed of the cation-s orbitals whose widespread character provides low effective masses. On the other hand, it is challenging to obtain p-type conductivity with these oxides because their valence bands are mainly formed by the O-2p orbitals, which results in deep valence band positions and relatively high effective masses. To remedy this, Kawazoe and Hosono *et al.* [8,9] have proposed the design principle that utilizes cations with the s^2 or d^{10} electronic configurations or mixed-anion systems, where cation or anion states are located near or above the O-2p states. Hybridizing the O-2p orbitals with other orbitals is expected to increase the position and dispersion of the valence band, which is a beneficial strategy for facilitating hole doping and lowering the hole effective mass. Several p-type TCOs have been found on the basis of this concept [10–14]. Prototypical examples are $CuMO_2$ (M = Al, Ga, In) [8,11,12] that crystallize in the delafossite structure. In particular, $CuInO_2$ attracted attention as a bipolar TCO capable of controlling the carrier type by selecting appropriate dopants [12]. However, $CuMO_2$ have not been put into practical use, which would be due to the limited conductivity associated with insufficient hole concentration and/or mobility. Nevertheless, it should be important to understand the electronic and defect properties of $CuMO_2$ for the design and exploration of superior p-type TCOs.

$CuAlO_2$ is most studied in this compound family, but there is still room for discussions about its band structure and defect properties. The indirect and direct band gaps of $CuAlO_2$ estimated by optical measurement are in the ranges of 1.65 to 2.99 eV [15–18] and 3.34 to 3.53 eV [8,17–19], respectively. First-principles studies of $CuAlO_2$ have also been conducted using various approximations [20–26]. The resultant theoretical band gap values significantly depend on the type and level of approximations used in the calculations. Furthermore, the exciton binding energy has been theoretically estimated to be as large as ~0.5 eV in $CuAlO_2$ [22], which would complicate the interpretation of optical absorption spectra to extract the fundamental band gap. In the modeling of semiconductors including their defect properties, the Heyd-Scuseria-Ernzerhof (HSE06) functional [27,28] based on the

*oba@msl.titech.ac.jp

hybrid Hartree-Fock density functional approach has been frequently used nowadays because it gives a relatively well-balanced description of electronic and structural properties of diverse materials [28–31]. The minimum gap values reported for $CuAlO_2$ are 3.52 [23] and 3.6 eV [25] using HSE06, which do not significantly deviate from the range of the reported experimental values and theoretical estimates using more elaborate approaches based on many-body perturbation theory [24]. Scanlon and Watson [23] discussed the behavior of point defects and the doping limits in $CuAlO_2$ using the results of HSE06 calculations. Their study revealed that the Cu vacancy (V_{Cu}) and the Cu-on-Al antisite (Cu_{Al}), which were thought to be responsible for the *p*-type conductivity, form deep defect levels associated with localized states.

Compared with $CuAlO_2$, there are fewer studies reported for $CuGaO_2$ and $CuInO_2$. According to experimental reports based on optical measurements, the minimum (indirect) band gaps of $CuGaO_2$ and $CuInO_2$ are 2.55 [32] and 1.44 eV [33], respectively. From the theoretical calculations using HSE06, their band gaps are predicted to be 2.4 and 1.6 eV [25], which show close agreement with the experimental values. However, the calculation of point defects at the hybrid functional level has not been reported except for the formation energies of the neutral vacancies [25]. Therefore, it is meaningful to comprehensively study the behavior of point defects in $CuGaO_2$ and $CuInO_2$ along with $CuAlO_2$, and obtain a basic perception of their roles in the carrier generation and compensation.

In this paper, we report on the energetics and electronic structures of native point defects in delafossite $CuMO_2$ ($M =$ Al, Ga, In) using first-principles calculations with the HSE06 hybrid functional. First, we revisit the bulk electronic properties of $CuMO_2$. Next, we investigate the native point defects in $CuMO_2$ and identify which defect species are relevant to the carrier generation and compensation. Our investigation goes into the local atomic structures and electronic states of the major defects, and the quantities pertaining to the generalized Koopmans' theorem (gKT) [34,35], the fulfillment of which is considered important for impartially describing localized defect states [36]. Finally, we comprehensively discuss the tendency in the defect properties of $CuMO_2$ and their doping limits determined by defect-induced carrier compensation in terms of the band edge positions.

II. COMPUTATIONAL DETAILS

The first-principles calculations were performed using the projector augmented-wave (PAW) method [37] with the HSE06 hybrid functional containing the Fock-exchange parameter α of 0.25 and the screening parameter μ of 0.21 Å^{-1} [27,28], as implemented in the VASP code [29,38,39]. We used PAW data sets with radial cutoffs of 1.22, 1.01, 1.38, 1.64, and 0.80 Å for Cu, Al, Ga, In, and O, respectively. Cu 3*d*, 4*s*, and 4*p*, Al 3*s* and 3*p*, Ga 4*s* and 4*p*, In 5*s* and 5*p*, and O 2*s* and 2*p* were described as valence electrons; Ga 3*d* and In 4*d* were treated as core electrons. The lattice vectors and internal atomic coordinates of the delafossite primitive unit cells were relaxed until the residual stresses and atomic forces converged to less than 0.025 GPa and 0.005 eV/Å, respectively. Monkhorst-Pack *k*-point meshes [40] of $8 \times 8 \times 8$ were used with a plane-wave cutoff energy of 520 eV in the geometry optimization. The band structure, density of states (DOS), and complex dielectric functions were evaluated using a plane-wave cutoff energy of 400 eV at the optimized geometry. For the DOS and complex dielectric function calculations, Γ-centered *k*-point meshes of $16 \times 16 \times 16$ were employed with downsampling by a factor of 2 for the Fock-exchange potential. The absorption spectra were obtained from the complex dielectric functions, which were based on the independent particle approximation without excitonic effects [41], and phonon-assisted indirect transitions were not considered. The band-averaged effective mass tensor was calculated using the BoltzTraP2 code [42], where the carrier concentration and temperature were set at 10^{16} cm^{-3} and 300 K, respectively, and denser Γ-centered *k*-point meshes of $24 \times 24 \times 24$ were taken with downsampling by a factor of 3 for the Fock-exchange potential.

For the defect calculations, the vacancies (V_{Cu}, V_M, and V_O), the cation antisites (Cu_M and M_{Cu}), and the interstitials (Cu_i, M_i, and O_i) were modeled with 108-atom supercells that were constructed by the $3 \times 3 \times 1$ expansion of the conventional unit cells. The sites with the minimum all-electron charge densities in the perfect crystals of $CuMO_2$ were extracted using the pymatgen code [43] and adopted as the interstitial sites [Fig. 1(a)]. Atoms neighboring the defect in the initial geometry of each supercell were subjected to random displacements of up to 0.2 Å in order to eliminate symmetry constraints. The internal atomic coordinates were relaxed under the fixed lattice vectors until the atomic forces became smaller than 0.03 eV/Å. We used a $2 \times 2 \times 2$ *k*-point mesh and a plane wave cutoff of 400 eV and took spin polarization into account for all supercell calculations.

The formation energy of defect D in charge state q ($E_f[D^q]$) was evaluated as

$$E_f[D^q] = E[D^q] + E_{corr}[D^q] - E_p - \sum_i \Delta n_i \mu_i + q(\varepsilon_{VBM} + \Delta\varepsilon_F), \quad (1)$$

where $E[D^q]$ and E_p are the total energies of the supercell with defect D in charge state q and the prefect-crystal supercell, respectively. Δn_i is the difference in the number of the constituent *i*-type atom between the defect and perfect-crystal supercells and μ_i is the chemical potential of the *i*-type atom. We calculated Cu-M-O ternary chemical potential diagrams at 0 K and 0 Pa to determine the regions of μ_i in which $CuMO_2$ are stable in the single phases. The standard states were set to the Cu and M metals and the O_2 molecule. $\Delta\varepsilon_F$ is the Fermi level with respect to the energy level of the valence band maximum (VBM) ε_{VBM}. The extended Freysoldt-Neugebauer-Van de Walle (eFNV) scheme [44,45] was applied to evaluate the correction term of the supercell total energy $E_{corr}[D^q]$, which is due to the presence of artificial electrostatic interactions in the finite-sized supercell with a charged defect ($q \neq 0$). The static dielectric tensors of the host materials used for $E_{corr}[D^q]$ are given in the Appendix, along with a discussion on the cell-size dependence of the formation energies before and after cell-size corrections. The pydefect code [46] was used for handling and analyzing the defect calculations.

To evaluate the localized-versus-delocalized behavior of defect states based on the gKT, the nonlinearity Δ_{XC} is

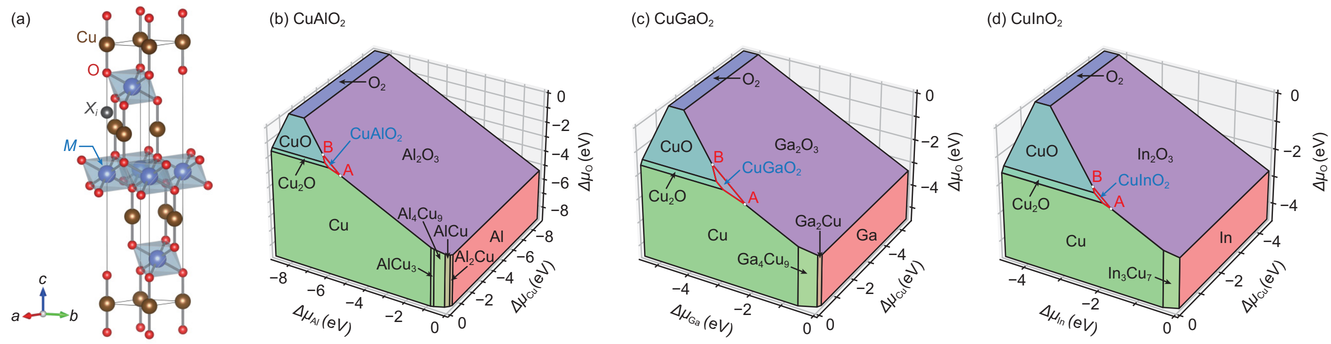

FIG. 1. (a) Crystal structure of delafossite CuMO$_2$ (M = Al, Ga, In). The interstitial site considered in the defect calculations is depicted as X_i. Chemical potential diagrams for (b) $CuAlO_2$, (c) $CuGaO_2$, and (d) $CuInO_2$ at 0 K and 0 Pa. The values of the chemical potentials are relative to those in the standard states, which are taken to be the Cu and M metals and the O_2 molecule. The regions surrounded by the red line represent the conditions of the chemical potentials where the single phases of CuMO$_2$ are stable, and their vertices and lines correspond to the extreme conditions where CuMO$_2$ coexist with other phases. Labels A and B indicate the O-poor and O-rich limits that are considered as two representative extreme cases, respectively.

introduced, which is defined as

$$\Delta_{XC} = E[D^{q+\Delta q}; \mathbf{R}^q] - E[D^q; \mathbf{R}^q] + \Delta E_{corr}^{VT} + \Delta q(\varepsilon[D^q; \mathbf{R}^q] + \varepsilon_{corr}[D^q; \mathbf{R}^q]), \quad (2)$$

where Δq is the additional charge of $+1$ or -1, $E[D^{q+\Delta q}; \mathbf{R}^q] - E[D^q; \mathbf{R}^q]$ can be thought of as the energy difference of the vertical transition from charge state q to $q + \Delta q$, and $\varepsilon[D^q; \mathbf{R}^q]$ is the single-particle level of the defect-induced localized state in the equilibrium atomic configuration $\mathbf{R}^q$. ΔE_{corr}^{VT} is the correction energy for the vertical transition, which is not the simple difference in those of the eFNV as described in Ref. [47]. $\varepsilon_{corr}[D^q; \mathbf{R}^q]$ is the correction term for the single-particle level of the localized state induced by a charged defect ($q \neq 0$) and can be written using the total-energy correction term as $\varepsilon_{corr}[D^q; \mathbf{R}^q] = -2E_{corr}[D^q; \mathbf{R}^q]/q$ [48]. We used the eFNV correction energy for $E_{corr}[D^q; \mathbf{R}^q]$ as in the case of the total energy correction. The gKT is satisfied when Δ_{XC} is zero. The localized/delocalized error increases as Δ_{XC} deviates from zero.

III. RESULTS AND DISCUSSION

A. Fundamental bulk properties

The crystal structure of delafossite CuMO$_2$ is shown in Fig. 1(a). It belongs to the rhombohedral lattice system with space group $R\bar{3}m$ and has only one equivalent site for each element. The structure of delafossite CuMO$_2$ is characterized by the layers composed of linear O-Cu-O bonds along the c direction and the MO_6 octahedron layers. The lattice constants for the delafossite conventional unit cells are listed in Table I. The theoretical and experimental values [49–51] are in good agreement within an error of ∼1%. Figures 1(b)–1(d) show the chemical potential diagrams of the Cu-M-O ternary systems used for determining the defect formation energies [Eq. (1)]. An antiferromagnetic ordering was assumed for CuO within the primitive unit cell containing two Cu atoms. The regions surrounded by the red line correspond to the conditions of the chemical potentials where the single phases of CuMO$_2$ are stable. In all the systems μ_{Cu} can vary in a narrow range where the μ_{Cu} values are generally close to that of the Cu metal. The variable ranges of μ_M and μ_O are much wider, and the differences in μ_M and μ_O between the two extreme conditions represented by points A and B are smaller in the order M = Ga, Al, and In: 1.34, 1.11, and 0.58 eV, respectively, for μ_M and 2/3 of these values for μ_O.

Figure 2 shows the electronic band structures, the total DOSs, and the DOSs projected on each of the atomic site and orbital for CuMO$_2$. It is clear that the upper part of the valence bands is mainly composed of Cu-d orbitals, which are hybridized with O-p orbitals, and the conduction bands are composed of Cu-p/d, O-p, and M-s orbitals in all the systems. The M-s orbitals dominate the electronic states near the conduction band minimum (CBM) more strongly in the order Al, Ga, and In, and the dispersion of the conduction band becomes larger in this order. The band-average effective mass tensors $\bar{m}$ of the electron and hole for CuMO$_2$ are shown in Table II along with the band gaps. In all the systems, the electron effective masses are relatively light. The values are $0.4m_0$–$0.5m_0$ except for the direction perpendicular to the c axis in $CuAlO_2$, where m_0 denotes the free-electron rest mass. The hole effective masses exhibit a large anisotropy. The values of $1.7m_0$–$1.9m_0$ in the direction perpendicular to the c axis are considered moderately small as p-type oxide semiconductors, whereas much larger values are found in the direction parallel to the c axis.

TABLE I. Lattice constants for the conventional unit cells of delafossite CuMO$_2$. The experimental values [49–51] and the percentage errors to those are also shown.

		$CuAlO_2$	$CuGaO_2$	$CuInO_2$
a (Å)	Calc.	2.856	2.984	3.326
	Expt.	2.860 [49]	2.977 [50]	3.292 [51]
	% error	−0.14	0.24	1.03
c (Å)	Calc.	16.961	17.190	17.446
	Expt.	16.953 [49]	17.171 [50]	17.388 [51]
	% error	0.05	0.11	0.33

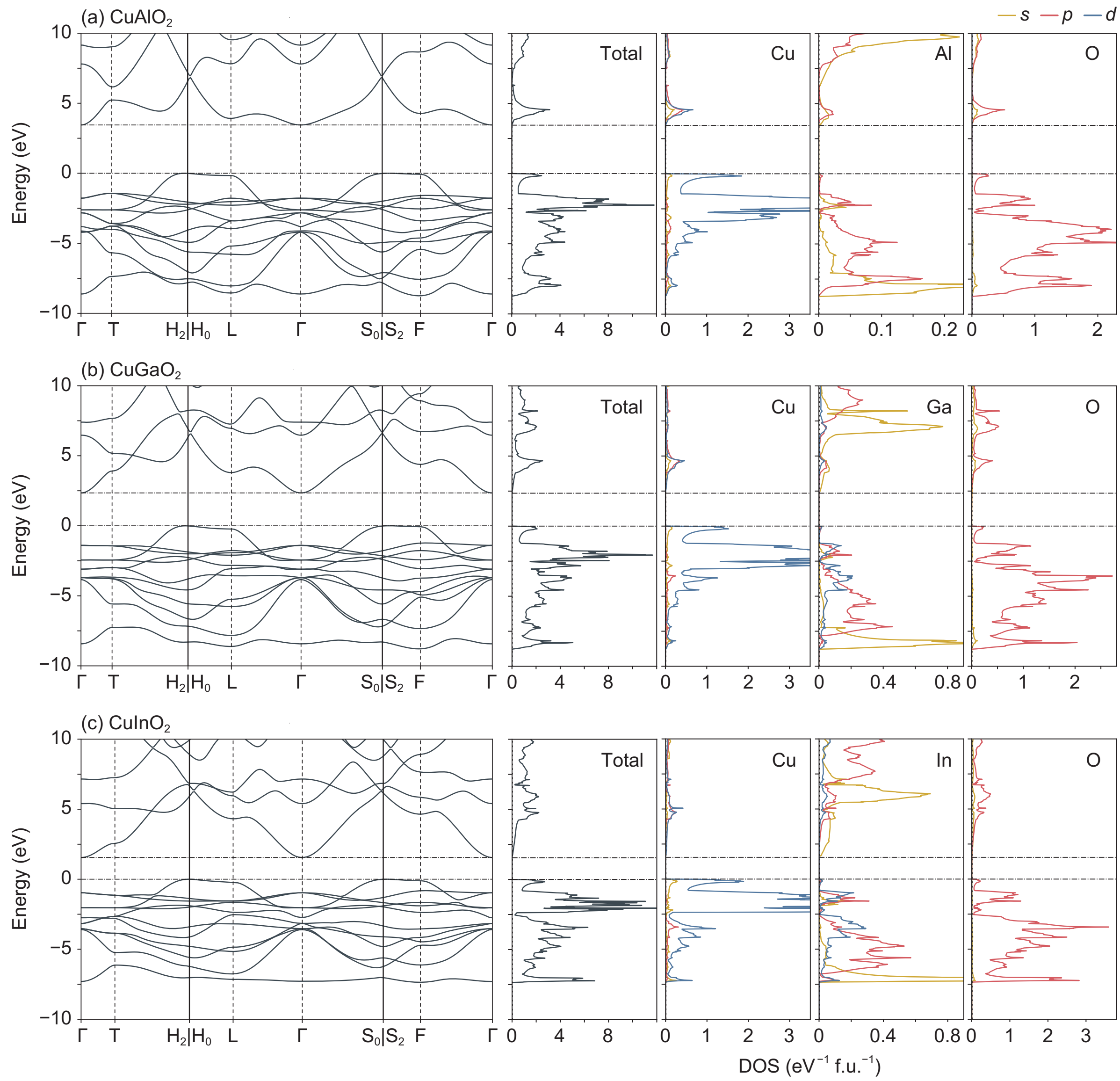

FIG. 2. Band structures, total DOSs, and the DOSs projected on each of the atomic site and orbital for (a) $CuAlO_2$, (b) $CuGaO_2$, and (c) $CuInO_2$. The band paths are determined using the seekpath code [52]. The VBMs are set to zero energies, which are indicated by the horizontal dashed lines as well as the CBMs.

Looking at the band structures, the CBMs are located at the Γ point in all the systems. The uppermost bands in the valence bands are rather flat around the VBMs, which are located at low symmetry points between the S_2 and F points. Thus, the band structures of CuMO$_2$ are of indirect type. Our theoretical indirect and direct band gaps summarized in Table II agree with the previously reported HSE06 results [23,25] within 0.15 eV. Regarding the indirect band gap, our theoretical values and the reported experimental values [32,33] are in reasonable agreement for $CuGaO_2$ and $CuInO_2$. The reported experimental indirect gap values for $CuAlO_2$ range from 1.65 to 2.99 eV [15–18], while our theoretical value of 3.45 eV is at least ∼0.5 eV larger. As mentioned in Sec. I, it has been reported that the theoretical band gap of $CuAlO_2$ is particularly sensitive to the type and level of approximations used in the calculations. Our value of 3.45 eV is close to the previously reported HSE06 values [23,25] and the reported quasiparticle gap using a self-consistent *GW* calculation including model polaronic corrections [24]. In addition, it has been pointed out that the experimental band gap could be underestimated because of the effects of defect levels [17,18,23]. For the direct band gap, the situation is complicated. Nie *et al.* have shown using first-principles calculations with the local density approximation (LDA) that CuMO$_2$ prohibit direct transitions at the Γ point and have high transition probabilities at the L and F points [20]. Since the Γ point gives the smallest direct band gaps in $CuGaO_2$ and $CuInO_2$, their absorption spectra slowly increase from the absorption edges determined by the direct transitions at the Γ point when excluding the effects of the indirect transitions. In our HSE06 results, the direct band gaps at the Γ point are also slightly and much smaller than those at the L and F points for $CuGaO_2$ and $CuInO_2$, respectively. The calculated absorption spectra are shown in Fig. 3. For all of CuMO$_2$, the absorption with the polarization

TABLE II. Indirect (E_g^{indir}) and direct (E_g^{dir}) band gaps, and band-average effective mass tensors of electron ($\bar{m}^e$) and hole ($\bar{m}^h$) for Cu$M$$O_2$. The reported experimental values of the band gaps [8,11,12,15–19,32,33,53] are also shown for comparison. E_g^{dir} at the Γ and L points are listed, at which the optical transitions are symmetrically forbidden and allowed, respectively. The band gaps are in eV. The effective masses are in the unit of the free-electron rest mass.

	$CuAlO_2$	$CuGaO_2$	$CuInO_2$
E_g^{indir}	3.45	2.35	1.55
E_g^{indir}(Expt.)	1.65 [15]	2.55 [32]	1.44 [33]
	1.8 [16]		
	2.97 [18]		
	2.99 [17]		
$E_g^{dir}(\Gamma)$	5.24	3.74	2.52
E_g^{dir}(L)	4.08	4.03	4.53
E_g^{dir}(Expt.)	3.34 [19]	3.6 [11]	3.9 [12]
	3.47 [18]	3.75 [32]	4.15 [53]
	3.5 [8]		4.45 [33]
	3.53 [17]		
$\bar{m}^e_{xx}$	1.16	0.50	0.43
$\bar{m}^e_{zz}$	0.38	0.39	0.51
$\bar{m}^h_{xx}$	1.93	1.70	1.75
$\bar{m}^h_{zz}$	5.52	4.71	10.5

perpendicular to the c axis is stronger near the absorption edges. The overall spectral features are consistent with the results reported by Nie *et al.* [20], Laskowski *et al.* [22], and Kumar *et al.* [25] using LDA, the Perdew-Burke-Ernzerhof functional within the generalized gradient approximation [54] with a Hubbard U [55] correction (PBE-GGA+U), and the HSE06 hybrid functional, respectively. Laskowski *et al.* estimated excitonic contribution to the optical absorption of Cu$M$$O_2$ by dealing with the electron-hole interaction in the framework of the Bethe-Salpeter formalism [22]. They found that a strong excitonic peak for the polarization perpendicular to the c axis appears at ~0.5 eV below the photon energy corresponding to the band gap value in $CuAlO_2$. In addition, the shapes of the imaginary part of the dielectric functions for the polarization perpendicular to the c axis are similar between $CuAlO_2$, $CuGaO_2$, and $CuInO_2$ in their report. This indicates that the strong excitonic peaks mainly appear near the absorption thresholds associated with the direct transitions at the L points in all of Cu$M$$O_2$. In our HSE06 results of the absorption spectra shown in Fig. 3, the absorption coefficients increase steeply to more than 10^5 cm^{-1} around photon energies of 4.1, 4.0, and 4.5 eV for $CuAlO_2$, $CuGaO_2$, and $CuInO_2$, respectively, corresponding to their direct band gaps at the L points given in Table II. Assuming that the exciton binding energies are ~0.5 eV for all of Cu$M$$O_2$, our calculated direct band gaps at the L point are almost consistent with the direct band gaps estimated from optical measurements, as compared in Table II.

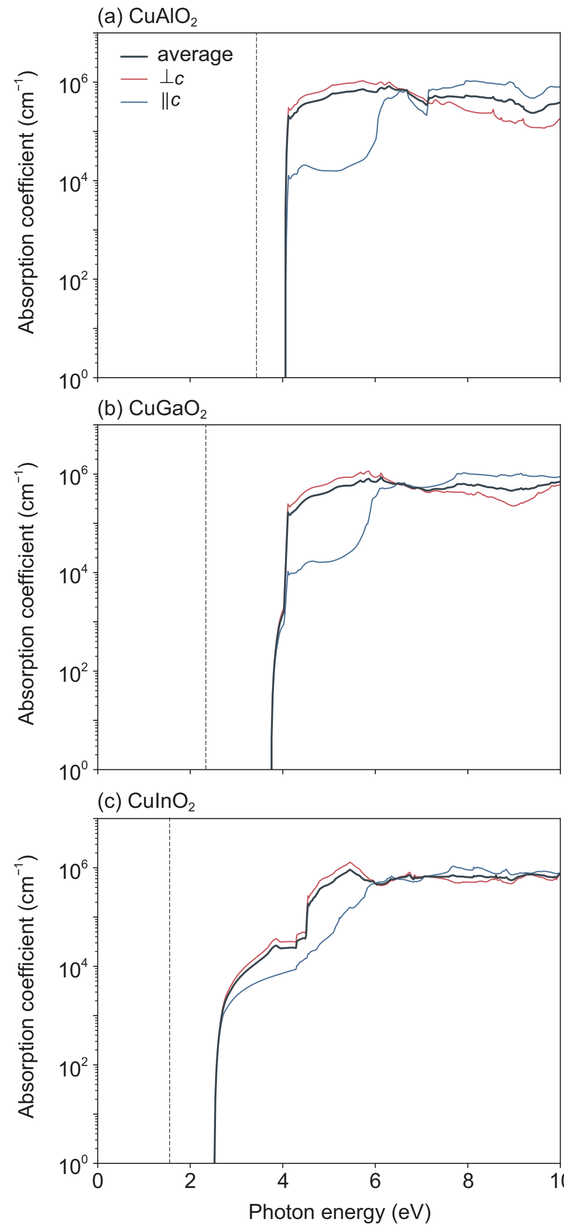

FIG. 3. Absorption spectra for (a) $CuAlO_2$, (b) $CuGaO_2$, and (c) $CuInO_2$. The black, red, and blue curves represent the spherically average and the components for the polarization perpendicular and parallel to the c axis, respectively. The dashed line indicates the minimum (indirect) band gaps.

B. Defect energetics

We now discuss the energetics of the native point defects of Cu$M$$O_2$. Figures 4(a)–4(c) show the formation energy diagrams for Cu$M$$O_2$ at the O-poor chemical potential conditions [corresponding to conditions A in Figs. 1(b)–1(d)]. The formation energies of the donor-type defects (V_O, M_{Cu}, Cu_i, and M_i) are generally high in $CuAlO_2$ and $CuGaO_2$. These defects tend to show lower formation energies in $CuInO_2$. In particular, the formation energy of Cu_i is much lower in $CuInO_2$, which can be attributed to the larger vacant space at the interstitial site. The same tendency can be seen for M_i, even though the ionic size is especially large for In. Note, however, that the formation energy of M_i depends on μ_M and the comparison between the interstitials with the different element species is not straightforward. On the other hand, although the μ_O values

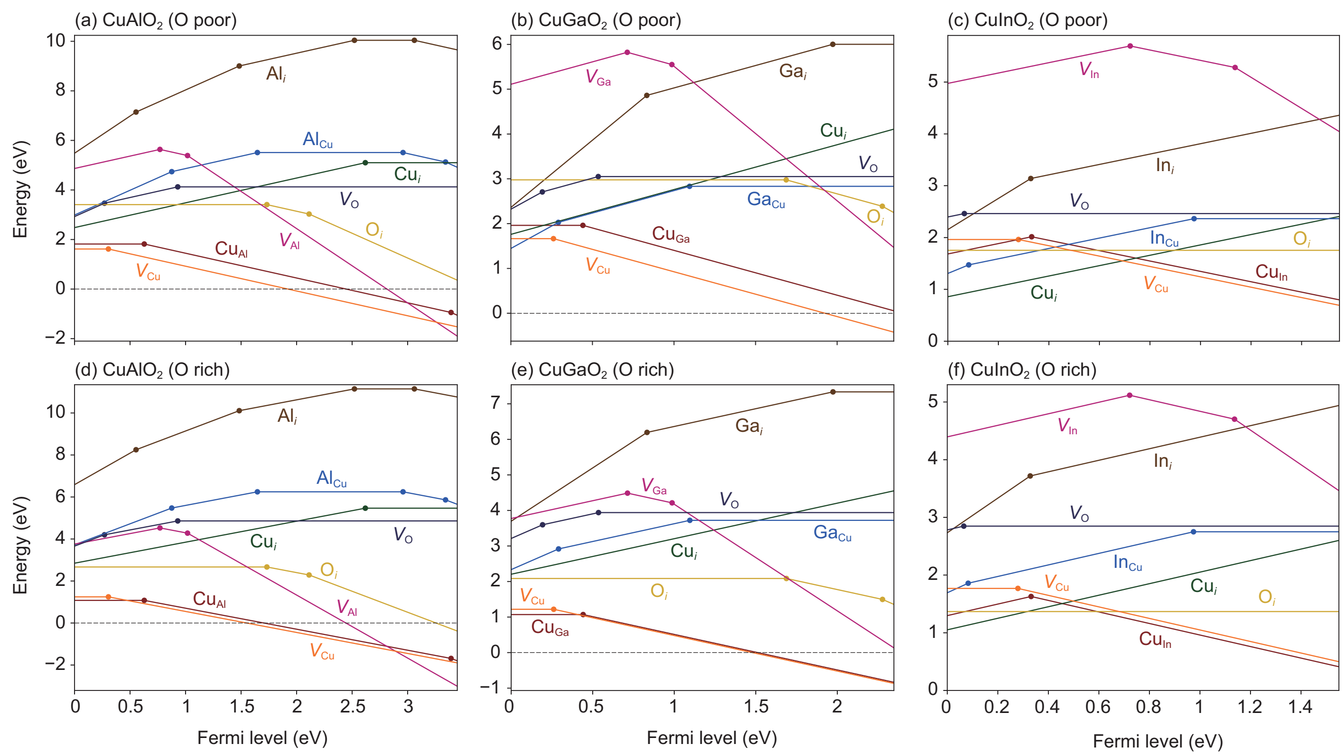

FIG. 4. Formation energies of native point defects in $CuAlO_2$ [(a) and (d)], $CuGaO_2$ [(b) and (e)], and $CuInO_2$ [(c) and (f)]. The O-poor chemical potential conditions [corresponding to conditions A in Figs. 1(b)–1(d)] are assumed in (a)–(c), and the O-rich chemical potential conditions [corresponding to conditions B in Figs. 1(b)–1(d)] are considered in (d)–(f). The type of defect is indicated by X_Y, where X is a vacancy (V) or element and Y is the defect site (i means the interstitial site). The range of the Fermi level is given by the VBM, which is set to zero, and the CBM in each system. For each defect, the formation energy in the most stable charge state at a Fermi level position is plotted, and the slope of the line corresponds to the defect charge state as defined in Eq. (1). The thermodynamic transition levels, corresponding to the Fermi level positions where the energetically preferred defect charge states change, are shown as filled circles.

under condition A are almost the same between the three systems, the formation energy of V_O decreases in the order M = Al, Ga, and In. Focusing on the thermodynamic transition levels, the donor-type defects except Cu_i in $CuGaO_2$ and $CuInO_2$ form deep donor levels. Cu_i in $CuGaO_2$ and $CuInO_2$, as well as In_i in $CuInO_2$, take the +1 charge states for the Fermi level position at the CBM. This indicates their shallow donor behaviors associated with hydrogenic donor states although such states with large spatial distributions cannot be described within the supercells used in this study. These donor-type defects, however, should not be major sources of carrier electrons as their formation energies are high at high Fermi level positions. Turning to the acceptor-type defects (V_{Cu}, V_M, Cu_M, and O_i), the formation energies of V_{Cu} and Cu_M are rather low or even negative at high Fermi level positions in $CuAlO_2$ and $CuGaO_2$. Carrier electrons should be strongly compensated by these defects even if extrinsic donor doping is conducted. Only $CuInO_2$ has no acceptor-type defects that have negative formation energy throughout the entire range of the Fermi level; therefore, it is capable of n-type doping in the presence of appropriate dopants, which is consistent with the experimental observation [12].

Figures 4(d)–4(f) show the formation energy diagrams at the O-rich chemical potential conditions [corresponding to conditions B in Figs. 1(b)–1(d)]. The formation energies of the acceptor-type defects (V_{Cu}, V_M, Cu_M, and O_i), which are associated with cation deficiency or O excess, are lowered compared with the O-poor conditions considered in Figs. 4(a)–4(c). Among them, V_{Cu} and Cu_M are the major defects with low formation energies, which is consistent with the HSE06 results for $CuAlO_2$ reported by Scanlon and Watson [23]. V_{Cu} forms the $(-1/0)$ acceptor levels, where the charge state changes between -1 and 0, at 0.30, 0.26, and 0.28 eV above the respective VBMs for $CuAlO_2$, $CuGaO_2$, and $CuInO_2$, and would contribute to hole generation. Cu_M forms deeper acceptor levels at 0.63 and 0.44 eV for $CuAlO_2$ and $CuGaO_2$, respectively. In $CuInO_2$, Cu_{In} shows the negative-U behavior and forms the transition level between the $+1$ and -1 charge states at 0.33 eV above the VBM. Therefore, Cu_{In} is likely to compensate holes when the Fermi level is close to the VBM, as well as donor-type Cu_i with an even lower formation energy. These results suggest that $CuInO_2$ cannot be an intrinsic p-type semiconductor with a high hole density. Fortunately, there are no donor-type defects that have negative energy throughout the entire Fermi level range in all of $CuMO_2$, and extrinsic hole doping is feasible if appropriate dopants exist. In addition, V_{Cu} and Cu_M can be the primary origins of the intrinsic p-type behavior of $CuAlO_2$ and $CuGaO_2$ since no substantial hole compensation by the donor-type defects is expected in these systems. The other acceptor-type defects (V_M and O_i) show high formation energies at low Fermi level positions and form very deep or no acceptor levels. Therefore, these defects cannot be the major sources of carrier holes. The formation energy of V_M

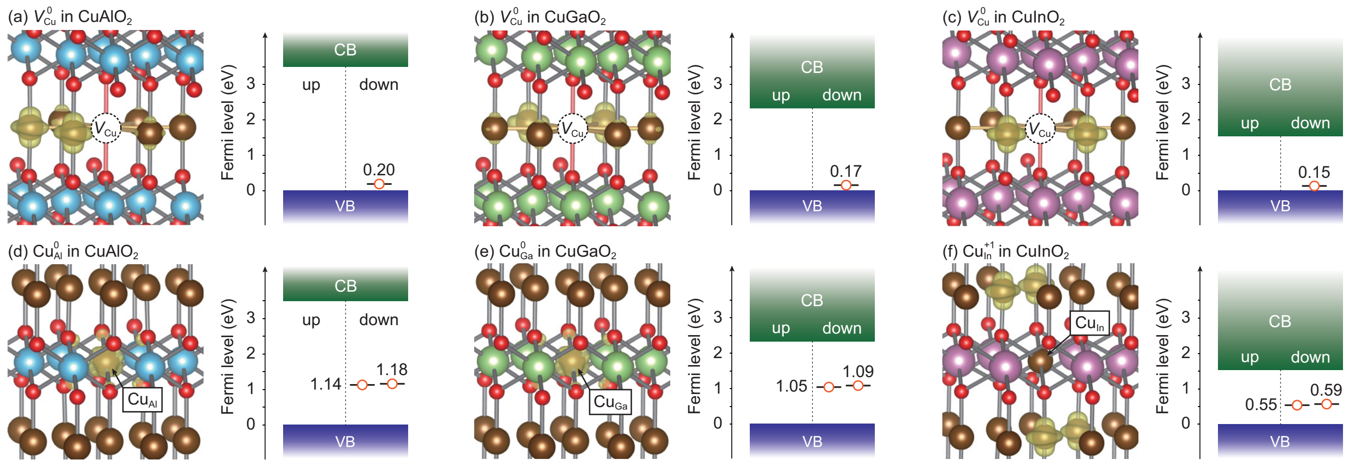

FIG. 5. Relaxed atomic configurations and isosurfaces of the squared wave functions of defect-induced in-gap states for $V_{\rm Cu}^0$ in (a) $CuAlO_2$, (b) $CuGaO_2$, and (c) $CuInO_2$ and for (d) $Cu_{\rm Al}^0$ in $CuAlO_2$, (e) $Cu_{\rm Ga}^0$ in $CuGaO_2$, and (f) $Cu_{\rm In}^{+1}$ in $CuInO_2$. The sum of the squared wave functions of two defect-induced in-gap states is taken for (d), (e), and (f). The single-particle levels of the defect-induced in-gap states for each spin are also shown on the right of the figures, where the VBMs are set to zero energies. Note that the other hole state for $Cu_{\rm In}^{+1}$ in $CuInO_2$ is buried in the conduction band and not shown in (f). Brown, blue, green, purple, and red balls indicate Cu, Al, Ga, In, and O atoms, respectively. The six bonds with the Cu atoms and the two bonds with the O atoms for the Cu atoms removed to form $V_{\rm Cu}$ are shown in orange and red, respectively. The isosurfaces correspond to 10% of the respective maximum values.

is low when the Fermi level is high, particularly in $CuAlO_2$, indicating their contributions to carrier electron compensation. As in the case of Cu_i, the formation energy of O_i decreases as the vacant space increases in the order M = Al, Ga, and In. The positions of the transition levels of O_i with respect to the respective VBMs are almost the same between $CuAlO_2$ and $CuGaO_2$. Unlike them, the transition levels of O_i in $CuInO_2$ are buried in the conduction band, and consequently, O_i^0 is most stable at any Fermi level.

C. Local structures and electronic states of acceptor-type defects

As discussed in Sec. III B, there are no native defect species in CuMO_2 that significantly contribute to the generation of carrier electrons, while $V_{\rm Cu}$ and Cu_M would contribute to hole generation. Therefore, we focus on $V_{\rm Cu}$ and Cu_M to discuss their local structures and electronic states. Figures 5(a)–5(c) show the relaxed atomic configurations and isosurfaces of the squared wave functions of defect-induced in-gap states for $V_{\rm Cu}^0$ in CuMO_2. The relaxed atomic configuration and electronic structure of $V_{\rm Cu}^0$ in $CuAlO_2$ have previously been investigated by Scanlon and Watson [23]. They reported that the six Cu atoms surrounding $V_{\rm Cu}$ relax inward by ∼0.01 Å, and the O atoms forming the linear O-Cu-O bond relax outward by ∼0.05 Å, and an excess hole is localized mainly on the former with *d*-like states. Our results show slight anisotropic behavior although the amounts of atomic relaxation are as small as those reported by Scanlon and Watson: the two O relax outward by ∼0.04 Å, and the four Cu relax inward by ∼0.01 Å and two Cu by ∼0.02 Å. The anisotropic configuration is marginally more stable than the isotropic one by 0.05 eV/supercell. Analysis of the squared wave functions of defect-induced in-gap states found that the hole is mainly localized on the two Cu atoms relaxed inward [Fig. 5(a)] with *d*-like states. The results for $CuGaO_2$ and $CuInO_2$ are similar to those for $CuAlO_2$, but the anisotropy slightly increases as M changes from Al and Ga to In. Such a localized state of the hole with the small amounts of atomic relaxation is not so common to metal oxides [56] and may be unique to Cu(I) compounds. The single-particle level of the defect-induced in-gap state for $V_{\rm Cu}^0$ in CuMO_2 does not vary much with M [Figs. 5(a)–5(c)], which is consistent with the trend of the $(-1/0)$ thermodynamic transition level.

Figures 5(d) and 5(e) show the relaxed atomic configuration and isosurfaces of the sum of the squared wave functions of the defect-induced in-gap states for $Cu_{\rm Al}^0$ in $CuAlO_2$ and $Cu_{\rm Ga}^0$ in $CuGaO_2$. $Cu_{\rm In}^0$ in $CuInO_2$ is excluded because it is unstable against the +1 and −1 charge states as discussed above, and $Cu_{\rm In}^{+1}$ is shown instead, whose single-particle levels of the defect-induced in-gap states are corrected as described in Sec. II [Fig. 5(f)]. In both cases of $Cu_{\rm Al}^0$ and $Cu_{\rm Ga}^0$, the two holes are mainly localized on $Cu_{\rm Al}^0$ and $Cu_{\rm Ga}^0$ with *d*-like states. Along with the cation substitution and the hole localization, the six neighboring O atoms relax outward almost isotropically by ∼0.07 and ∼0.01 Å for $CuAlO_2$ and $CuGaO_2$, respectively. The average bond distance between Cu_M^0 and the O atoms becomes 1.98 and 2.01 Å for M = Al and Ga, respectively. Since the electrostatic interaction between the positively charged Cu_M and the negatively charged nearby O atoms is inversely proportional to the bond distance, the electrostatic energy gain is expected to be greater for M = Al with a shorter bond distance. In addition, the average positions of the defect-induced in-gap single-particle levels are 1.16 and 1.07 eV, with respect to the VBMs, for $Cu_{\rm Al}^0$ in $CuAlO_2$ and $Cu_{\rm Ga}^0$ in $CuGaO_2$, respectively. These features in atomic geometry and single-particle levels are consistent with the fact that the $(-1/0)$ thermodynamic transition level of Cu_M in $CuAlO_2$ is deeper than that in $CuGaO_2$. Unlike $Cu_{\rm Al}^0$ in $CuAlO_2$ and $Cu_{\rm Ga}^0$ in $CuGaO_2$, $Cu_{\rm In}^{+1}$ in $CuInO_2$ forms in-gap states with two holes distributed on four neighboring Cu atoms [Fig. 5(f)]. The other hole state is buried in the conduction band, which is not shown in Fig. 5(f). As can be seen from Fig. 2, the width of the Cu-3d bands of $CuInO_2$ is narrower than those of the other systems, which may facilitate the localization of holes on the host Cu atoms. The average position of the in-gap single-particle levels of Cu_{In}^{+1} is 0.57 eV above the VBM, which is relatively shallower than those of Cu_{Al}^0 in $CuAlO_2$ and Cu_{Ga}^0 in $CuGaO_2$.

To investigate how close the HSE06 functional to the gKT condition for these localized defect states, Δ_{XC} is estimated based on Eq. (2) using the unoccupied single-particle level of the defect-induced in-gap state $\varepsilon[D^0; \mathbf{R}^0]$, and the difference between the total energies after and before the addition of an electron $E[D^{-1}; \mathbf{R}^0] - E[D^0; \mathbf{R}^0]$. We do not discuss the gKT for Cu_{In} in $CuInO_2$ because of the instability of the neutral charge state. For Cu_{Al} in $CuAlO_2$ and Cu_{Ga} in $CuGaO_2$, Δ_{XC} is 0.05 and -0.06 eV, respectively, which almost satisfies the gKT. On the other hand, Δ_{XC} is 0.42, 0.39, and 0.43 eV for V_{Cu} in $CuAlO_2$, $CuGaO_2$, and $CuInO_2$, respectively. This implies that the optimal conditions are different for defect species as in the case of Ref. [57], and the description of the V_{Cu}-induced states is biased toward delocalization. Therefore, we searched for α that satisfies the gKT for V_{Cu} in $CuMO_2$, using the relaxed geometries and the dielectric tensors for the cell-size corrections obtained using the HSE06 functional ($\alpha = 0.25$). The results show that for all the systems, $\Delta_{XC} \simeq 0$ at $\alpha = 0.40$, and $E[V_{Cu}^{-1}; \mathbf{R}^0] - E[V_{Cu}^0; \mathbf{R}^0]$ is nearly constant across the considered range of the α value (Fig. 6). Assuming that the structural relaxation energy, $E[V_{Cu}^{-1}; \mathbf{R}^{-1}] - E[V_{Cu}^{-1}; \mathbf{R}^0]$, and the equilibrium geometries, $\mathbf{R}^0$ and $\mathbf{R}^{-1}$, are independent of α, the absolute position of the acceptor level is also independent of α, as in the case of a self-trapped hole level in β-Ga_2O_3 [58]. Furthermore, we performed a series of calculations using HSE($\alpha = 0.40$), including the structure relaxation and dielectric tensor evaluation, and conducted the same assessment for V_{Cu}. It is found that the topology of the hole localization is almost unchanged from that of HSE06 with $\alpha = 0.25$ [Figs. 5(a)–5(c)] in all the systems, and Δ_{XC} and the minimum band gaps are -0.02, -0.05, and -0.05 eV and 4.52, 3.44, and 2.52 eV for $CuAlO_2$, $CuGaO_2$, and $CuInO_2$, respectively. Thus, HSE($\alpha = 0.40$) almost satisfies the gKT for V_{Cu} but yields band gaps significantly larger than the HSE06 values. It is obvious that the absolute value of the VBM is important for determining the position of the acceptor level. The ionization potential (IP) and electron affinity (EA), corresponding to the positions of the VBM and CBM with respect to the vacuum level, respectively, are often used to discuss the absolute positions of the band edges, but the comparison of the IP and EA between theory and experiment is often not straightforward because they strongly depend on the surface orientation and geometry, defects, and adsorption via the contribution of the surface dipoles [59–62]. Thus, accurate prediction of the acceptor level positions with respect to the band edges is challenging even though the absolute positions of the acceptor levels are robust against the convex/concave behavior of the functional. In the present study we base our discussion on the band edges obtained using HSE06, which provides reasonable estimates of the band gaps of $CuMO_2$ as mentioned above and the IP of $CuAlO_2$ as will be discussed in Sec. III D.

Focusing on the α dependence of $\varepsilon[V_{Cu}^0; \mathbf{R}^0]$, the absolute position of $\varepsilon[V_{Cu}^0; \mathbf{R}^0]$ becomes deeper with respect to the VBM as α increases. Specifically, for HSE($\alpha = 0.40$), which almost satisfies the gKT $\varepsilon[V_{Cu}^0; \mathbf{R}^0]$ is ~0.3 eV deeper than that of HSE06 in all of $CuMO_2$. From this perspective, we emphasize that particular care for the gKT is needed when discussing based on the single-particle level rather than the total energy-based thermodynamic transition level. The positions of $\varepsilon[V_{Cu}^0; \mathbf{R}^0]$ shown in Figs. 5(a)–5(c) are no exception and should be much deeper when the gKT is satisfied to remove the delocalization error. In that case, $\varepsilon[V_{Cu}^0; \mathbf{R}^0]$ is expected to

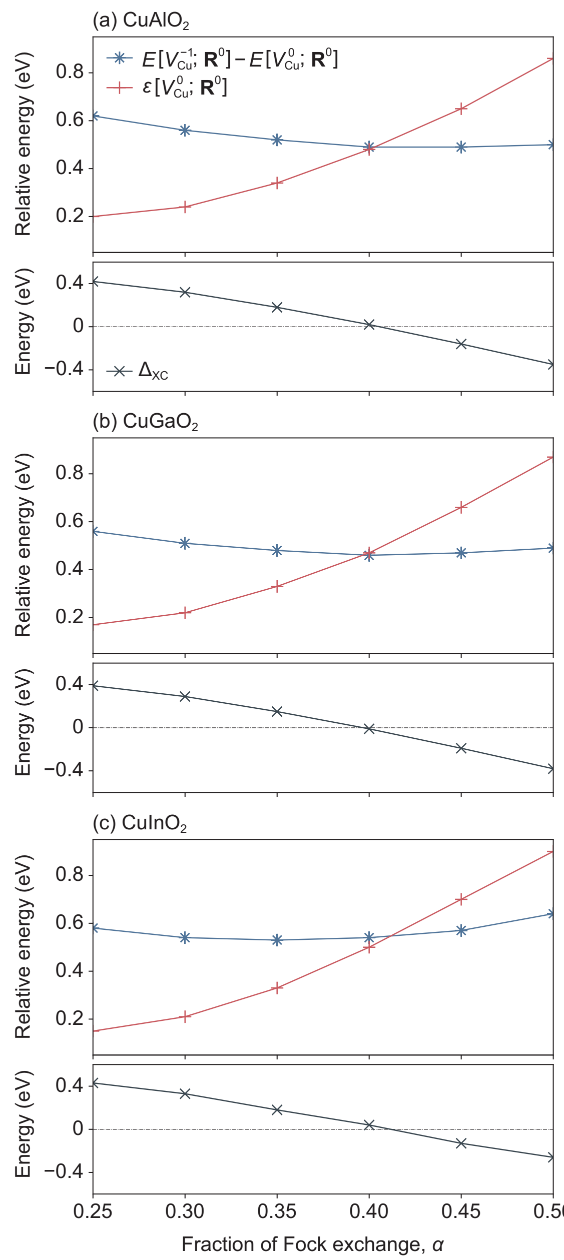

FIG. 6. Dependence of the gKT-relevant quantities on the Fock-exchange parameter α in the HSE hybrid functional for V_{Cu} in (a) $CuAlO_2$, (b) $CuGaO_2$, and (c) $CuInO_2$. The relaxed geometries and the dielectric tensors for the cell-size corrections obtained using the HSE06 functional ($\alpha = 0.25$) are used in all cases. Positive and negative values for Δ_{XC} mean that the delocalization and localization errors remain, respectively. $E[V_{Cu}^{-1}; \mathbf{R}^0] - E[V_{Cu}^0; \mathbf{R}^0]$ and $\varepsilon[V_{Cu}^0; \mathbf{R}^0]$ are relative values to the VBM obtained using HSE06.

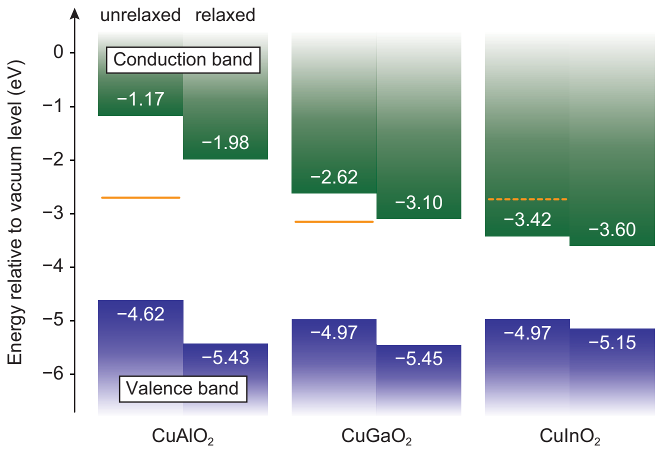

FIG. 7. Band edge positions of CuMO$_2$ (11$\bar{2}$0) surfaces with respect to the vacuum level. For each system, the results with unrelaxed and relaxed internal coordinates are shown on the left and right. The n-type doping limits, namely the upper limits of the Fermi level in thermodynamic equilibrium, determined by V_{Cu}, are shown by the orange lines only for the unrelaxed cases, excluding the relaxation contributions to the surface dipole effects from the band alignment. When the Fermi level is higher than these lines, V_{Cu}^{-1} is formed spontaneously to compensate carrier electrons.

be almost constant in CuMO$_2$ as in the HSE06 results shown in Figs. 5(a)–5(c) since HSE06 yields almost the same Δ_{XC} for V_{Cu} in the three systems.

D. Doping limits

Finally, we discuss the cause of the difference in the carrier dopability of CuMO$_2$ in terms of carrier compensation by charged native point defects. As mentioned in Sec. III C, the hole compensation by the donor-type native defects does not essentially limit the p-type doping in all of CuMO$_2$. In contrast, the acceptor-type native defects, especially V_{Cu}, show low or negative formation energies at high Fermi level positions even under O-poor chemical potential conditions, thereby compensating carrier electrons to limit the n-type doping. Although native defect formation can be kinetically suppressed in part under nonequilibrium growth and/or doping conditions, we base our discussion on the thermodynamic equilibrium cases here.

The relative positions of the band edges and the n-type doping limits, namely the upper limits of the Fermi level in thermodynamic equilibrium, determined by V_{Cu} are depicted in Fig. 7. The position of the band edge has been reported to be a good indicator of the carrier dopability, with a high VBM position facilitating hole doping and a low CBM position facilitating electron doping [9,20,63–65]. In order to compare the positions of the band edges between different systems, the IPs and EAs of the three systems are determined by using the method combining the bulk and slab-vacuum model [31]. We constructed slab-vacuum models of the nonpolar (11$\bar{2}$0) surfaces for CuMO$_2$ containing 32 atoms with slab and vacuum thicknesses of both ~10 Å using the procedure described in Ref. [66] and calculated the differences in the electrostatic potentials of the vacuum region and the bulklike region in the slab in two cases with and without relaxation of the internal coordinates. The IPs and EAs for the unrelaxed and relaxed surfaces were finally obtained by adopting the electrostatic potentials of the bulk and bulklike region in the slab as a common reference. Relaxation of the surface internal coordinates leads to a downward shift of the band edges by 0.81, 0.48, and 0.18 eV for $CuAlO_2$, $CuGaO_2$, and $CuInO_2$, respectively. The resultant IP value of 5.43 eV for $CuAlO_2$ is close to the experimentally reported value of ~5 eV [9]. Since the IP and EA are considerably dependent on the surface geometry as well as its orientation due to the contribution of the surface dipole as mentioned in Sec. III C, we discuss the doping limits based on the unrelaxed results. For CuMO$_2$, however, the surface relaxation does not significantly affect the relative band edge positions as shown in Fig. 7.

The positions of the VBMs for the three systems are close to each other, as expected from the similar chemical bonding states in their valence bands, as well as the common crystal structure and similar chemical compositions. Therefore, from the viewpoint of the VBM position, there is not much difference in the p-type dopability of CuMO$_2$, which is consistent with the fact that p-type doping is realized in all the systems [8,11,12]. On the other hand, the positions of the CBMs differ greatly between the three systems: as M changes from Al to Ga and In, the CBM shifts downward on the order of a few eV. These tendencies in the band alignment are similar to those reported by Nie *et al.* using the LDA [20]. This implies that the introduction of carrier electrons becomes easier in the order M = Al, Ga, and In. It can also be seen from Fig. 7 that the n-type doping limits determined by V_{Cu} in CuMO$_2$ are almost constant among all the systems. This means that under the O-poor chemical potential conditions, the formation energy of V_{Cu} is almost independent of the system at the common Fermi level position with respect to the vacuum level. As a result, the n-type doping limit by V_{Cu} is located above the CBM in only $CuInO_2$, which is consistent with the fact that n-type doping has thus far been achieved in only $CuInO_2$ [12]. Thus, the CBM position is a good indicator of the n-type doping limits in CuMO$_2$, as proposed previously [9,20,63–65], and can be used as a guideline for designing CuMO$_2$ alloys and related Cu(I) oxides.

IV. CONCLUSIONS

We have theoretically investigated the properties of the native point defects in CuMO$_2$ using the HSE06 hybrid functional, along with fundamental bulk properties. The calculated band gaps show reasonable agreement with the experimental values when the optical transitions are interpreted on the basis of the previous reports. The band-average effective masses of electrons are relatively low in the direction parallel to the c axis in all of CuMO$_2$ and nearly isotropic in $CuGaO_2$ and $CuInO_2$. In all of CuMO$_2$, the hole effective masses are moderately low in the direction perpendicular to the c axis, while high in the direction parallel to the c axis.

The energetics of the native point defects in CuMO$_2$ suggests that there are no shallow donor defects with low formation energies. Carrier compensation due to the formation of V_{Cu} and Cu_M is likely to be substantial for $CuAlO_2$ and $CuGaO_2$, but not for $CuInO_2$. For the acceptor-type defects,

V_{Cu} is found to be the primary contributor to the hole generation because it exhibits relatively shallow acceptor level and low formation energy. Furthermore, there are no donor-type native defects that strongly compensate holes. The analysis of the electronic states of V_{Cu} and Cu_M show that the introduced holes are localized in d-like states on the Cu atoms neighboring V_{Cu} and the Cu_M antisite atoms, respectively. The degree of localization of these major acceptor-type defects is discussed in terms of the gKT. It is found that the gKT is almost satisfied by HSE06 for $\mathrm{Cu_{Al}}$ in $\mathrm{CuAlO_2}$ and for $\mathrm{Cu_{Ga}}$ in $\mathrm{CuGaO_2}$ and by HSE($\alpha = 0.40$) for V_{Cu} in all of $\mathrm{Cu}M\mathrm{O_2}$. The conditions satisfying the gKT thus depend on the defect species, but the absolute positions of the acceptor levels are robust against α. The relative positions of the band edges and the Fermi-level upper limits are compared in the band alignment with respect to the vacuum level. The VBM positions of $\mathrm{Cu}M\mathrm{O_2}$ are close to each other, whereas their CBM positions are significantly different and lower in the order M = Al, Ga, and In. Furthermore, the Fermi-level upper limits determined by the carrier compensation by V_{Cu} are almost constant throughout all the systems. These results indicate that the position of the CBM is an important indicator of the n-type doping limits in $\mathrm{Cu}M\mathrm{O_2}$ as proposed previously.

ACKNOWLEDGMENTS

We sincerely thank Prof. Hiroshi Yanagi for fruitful discussions on the band structures of $\mathrm{Cu}M\mathrm{O_2}$. This work was supported by JSPS KAKENHI Grants No. JP20J23137 and No. JP20H00302, JST CREST Grant No. JPMJCR17J2, and the Design & Engineering by Joint Inverse Innovation for Materials Architecture project from MEXT. The computing resources of Academic Center for Computing and Media Studies at Kyoto University, Research Institute for Information Technology at Kyushu University, and National Institute of Advanced Industrial Science and Technology were used for part of this work. The crystal structures and the isosurfaces of the squared wave functions in Figs. 1(a) and 5 were drawn by using the VESTA code [67].

APPENDIX

Here, we summarize the methods for calculating the dielectric tensors and the values used for the cell-size corrections in the evaluation of the defect formation energies. The correction term $E_{\mathrm{corr}}[D^q]$ in Eq. (1) involves the static dielectric tensor of the host material that is given as the ion-clamped dielectric tensor (ϵ^{ele}), which is the sum of the vacuum permittivity and the electronic contribution, plus the ionic contribution (ϵ^{ion}). For the defect energetics in the main text, ϵ^{ele} was calculated using HSE06 with a finite-electric-field (FEF) approach [68]. PBE-GGA+U was used to evaluate ϵ^{ion} based on density-functional perturbation theory (DFPT) [41,69]. An effective U value of 5 eV was applied to the Cu-d orbitals based on the Dudarev's formalism [70]. Monkhorst-Pack k-point meshes of $16 \times 16 \times 16$ were used with a plane-wave cutoff energy of 400 eV for both calculations based on FEF and DFPT approaches; in the former, the k-point meshes were downsampled by a factor of 2 for the Fock-exchange potential.

The calculated ϵ^{ele} and ϵ^{ion} values are listed in Table III. Both ϵ^{ele} and ϵ^{ion} show a noticeable anisotropy in all the systems, where the values are smaller for the direction parallel to the c axis.

Next, we discuss the dependence of the formation energies on the supercell size, taking examples of V_{Cu}^{-1} and $\mathrm{Cu_{Al}^{-1}}$, which are dominant acceptor-type defects, and highly charged V_{Al}^{-3} in $\mathrm{CuAlO_2}$. The calculations were performed using the PBE-GGA+U with an effective U value of 5 eV for the Cu-d orbitals. Both ϵ^{ele} and ϵ^{ion} were calculated using PBE-GGA+U based on DFPT with Monkhorst-Pack

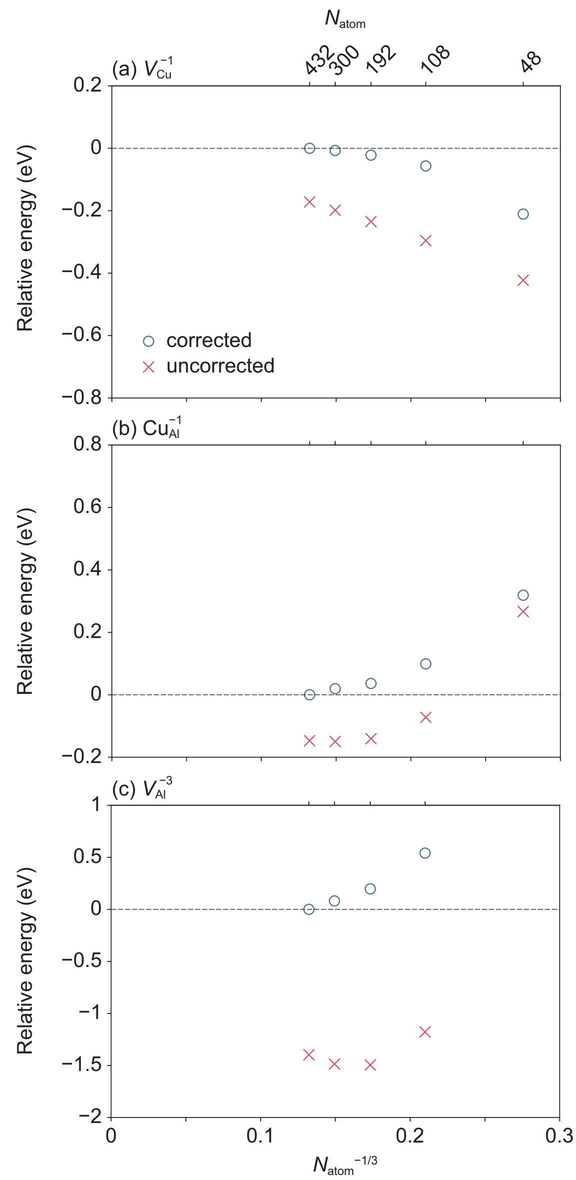

FIG. 8. Dependence of corrected and uncorrected formation energies on the supercell size for (a) V_{Cu}^{-1}, (b) $\mathrm{Cu_{Al}^{-1}}$, and (c) V_{Al}^{-3} in $\mathrm{CuAlO_2}$. N_{atom} is the number of atoms in the supercell. A $2 \times 2 \times 2$ k-point mesh is used for all sizes of the supercells. The energy zeros are set at the respective corrected values for the largest 432-atom supercells. The data for the 48-atom supercell of V_{Al}^{-3} are omitted because the electronic state is qualitatively different from that in the other supercells.

TABLE III. Ion-clamped dielectric tensors (ϵ^{ele}) and ionic contributions (ϵ^{ion}) for CuMO$_2$. The dielectric tensors calculated at the HSE06-optimized geometries were used for the cell-size corrections in the main text, and those calculated at the PBE-GGA+U-optimized geometries were used for the cell-size convergence tests on selected defects in $CuAlO_2$ (Fig. 8).

Theory/Method	Approximation for exchange correlation	Geometry	Component	$CuAlO_2$	$CuGaO_2$	$CuInO_2$
FEF	HSE06	HSE06	$\epsilon_{xx}^{\text{ele}}$	4.91	4.96	4.37
			$\epsilon_{zz}^{\text{ele}}$	3.80	3.98	3.75
DFPT	PBE-GGA+U	HSE06	$\epsilon_{xx}^{\text{ion}}$	4.54	4.31	2.98
			$\epsilon_{zz}^{\text{ion}}$	2.36	2.12	1.92
DFPT	PBE-GGA+U	PBE-GGA+U	$\epsilon_{xx}^{\text{ele}}$	4.93		
			$\epsilon_{zz}^{\text{ele}}$	4.33		
			$\epsilon_{xx}^{\text{ion}}$	4.82		
			$\epsilon_{zz}^{\text{ion}}$	2.42		

k-point meshes of 16 × 16 × 16 and a plane-wave cutoff energy of 400 eV, and the obtained values are listed in Table III. Figure 8 shows the corrected and uncorrected formation energies as a function of the supercell size. $E_f[V_{\text{Cu}}^{-1}]$ [Fig. 8(a)] and $E_f[\text{Cu}_{\text{Al}}^{-1}]$ [Fig. 8(b)] converge sufficiently within an error of 0.1 eV at the size of the 108-atom supercell, which was taken for the defect calculations using the HSE06 hybrid functional. On the other hand, for $E_f[V_{\text{Al}}^{-3}]$ [Fig. 8(c)], an error of 0.54 eV remains in the 108-atom supercell, even with the correction. This is due to the fact that the conventional unit cell of the delafossite structure has a relatively large c dimension, and the interdefect distance in the direction perpendicular to the c axis is not sufficient in the 108-atom supercell. The use of the 192-atom and 300-atom supercells can reduce the error to less than 0.20 and 0.08 eV, respectively, but the computational cost is too high to perform hybrid functional calculations using these supercells.

In summary, the formation energies of the highly charged defect species, such as V_{Al}^{-3}, would have errors of ~0.5 eV because of the limited supercell size. However, this degree of errors is unlikely to alter the conclusions of this paper. In addition, the formation energies of the major defects, such as V_{Cu}^{-1} and $\text{Cu}_{\text{Al}}^{-1}$, are considered well converged after the cell-size corrections.

[1] A. Facchetti and T. Marks, Eds., *Transparent Electronics: From Synthesis to Applications* (Wiley, New York, 2010).

[2] H. Ohta, M. Orita, M. Hirano, H. Tanji, H. Kawazoe, and H. Hosono, Appl. Phys. Lett. **76**, 2740 (2000).

[3] H. Randhawa, M. Matthews, and R. Bunshah, Thin Solid Films **83**, 267 (1981).

[4] R. Banerjee and D. Das, Thin Solid Films **149**, 291 (1987).

[5] T. Ishida, O. Tabata, J. il Park, S. H. Shin, H. Magara, S. Tamura, S. Mochizuki, and T. Mihara, Thin Solid Films **281**, 228 (1996).

[6] T. Minami, H. Nanto, and S. Takata, Appl. Phys. Lett. **41**, 958 (1982).

[7] T. Minami, H. Sato, H. Nanto, and S. Takata, Jpn. J. Appl. Phys. **24**, L781 (1985).

[8] H. Kawazoe, M. Yasukawa, H. Hyodo, M. Kurita, H. Yanagi, and H. Hosono, Nature (London) **389**, 939 (1997).

[9] H. Hosono, *Transparent Electronics: From Synthesis to Applications* (Wiley, New York, 2010), Chap. 2.

[10] A. Kudo, H. Yanagi, H. Hosono, and H. Kawazoe, Appl. Phys. Lett. **73**, 220 (1998).

[11] K. Ueda, T. Hase, H. Yanagi, H. Kawazoe, H. Hosono, H. Ohta, M. Orita, and M. Hirano, J. Appl. Phys. **89**, 1790 (2001).

[12] H. Yanagi, T. Hase, S. Ibuki, K. Ueda, and H. Hosono, Appl. Phys. Lett. **78**, 1583 (2001).

[13] H. Hiramatsu, K. Ueda, H. Ohta, M. Hirano, T. Kamiya, and H. Hosono, Appl. Phys. Lett. **82**, 1048 (2003).

[14] H. Hosono, Thin Solid Films **515**, 6000 (2007).

[15] F. Benko and F. Koffyberg, J. Phys. Chem. Solids **45**, 57 (1984).

[16] H. Yanagi, S.-i. Inoue, K. Ueda, H. Kawazoe, H. Hosono, and N. Hamada, J. Appl. Phys. **88**, 4159 (2000).

[17] J. Pellicer-Porres, A. Segura, A. Gilliland, A. Munoz, P. Rodríguez-Hernández, D. Kim, M. Lee, and T. Kim, Appl. Phys. Lett. **88**, 181904 (2006).

[18] J. Tate, H. L. Ju, J. C. Moon, A. Zakutayev, A. P. Richard, J. Russell, and D. H. McIntyre, Phys. Rev. B **80**, 165206 (2009).

[19] A. Banerjee and K. Chattopadhyay, J. Appl. Phys. **97**, 084308 (2005).

[20] X. Nie, S.-H. Wei, and S. B. Zhang, Phys. Rev. Lett. **88**, 066405 (2002).

[21] I. Hamada and H. Katayama-Yoshida, Phys. B: Condens. Matter **376**, 808 (2006).

[22] R. Laskowski, N. E. Christensen, P. Blaha, and B. Palanivel, Phys. Rev. B **79**, 165209 (2009).

[23] D. O. Scanlon and G. W. Watson, J. Phys. Chem. Lett. **1**, 3195 (2010).

[24] J. Vidal, F. Trani, F. Bruneval, M. A. L. Marques, and S. Botti, Phys. Rev. Lett. **104**, 136401 (2010).

[25] M. Kumar, H. Zhao, and C. Persson, Semicond. Sci. Technol. **28**, 065003 (2013).

[26] R. Gillen and J. Robertson, Phys. Rev. B **84**, 035125 (2011).

[27] J. Heyd, G. E. Scuseria, and M. Ernzerhof, J. Chem. Phys. **118**, 8207 (2003).

[28] A. V. Krukau, O. A. Vydrov, A. F. Izmaylov, and G. E. Scuseria, J. Chem. Phys. **125**, 224106 (2006).
[29] J. Paier, M. Marsman, K. Hummer, G. Kresse, I. C. Gerber, and J. G. Ángyán, J. Chem. Phys. **124**, 154709 (2006).
[30] Y. Hinuma, A. Grüneis, G. Kresse, and F. Oba, Phys. Rev. B **90**, 155405 (2014).
[31] F. Oba and Y. Kumagai, Appl. Phys. Express **11**, 060101 (2018).
[32] J. W. Lekse, M. K. Underwood, J. P. Lewis, and C. Matranga, J. Phys. Chem. C **116**, 1865 (2012).
[33] M. Sasaki and M. Shimode, J. Phys. Chem. Solids **64**, 1675 (2003).
[34] J. P. Perdew, R. G. Parr, M. Levy, and J. L. Balduz Jr., Phys. Rev. Lett. **49**, 1691 (1982).
[35] A. J. Cohen, P. Mori-Sánchez, and W. Yang, Science **321**, 792 (2008).
[36] S. Lany and A. Zunger, Phys. Rev. B **80**, 085202 (2009).
[37] P. E. Blöchl, Phys. Rev. B **50**, 17953 (1994).
[38] G. Kresse and J. Furthmüller, Phys. Rev. B **54**, 11169 (1996).
[39] G. Kresse and D. Joubert, Phys. Rev. B **59**, 1758 (1999).
[40] H. J. Monkhorst and J. D. Pack, Phys. Rev. B **13**, 5188 (1976).
[41] M. Gajdoš, K. Hummer, G. Kresse, J. Furthmüller, and F. Bechstedt, Phys. Rev. B **73**, 045112 (2006).
[42] G. K. Madsen, J. Carrete, and M. J. Verstraete, Comput. Phys. Commun. **231**, 140 (2018).
[43] S. P. Ong, W. D. Richards, A. Jain, G. Hautier, M. Kocher, S. Cholia, D. Gunter, V. L. Chevrier, K. A. Persson, and G. Ceder, Comput. Mater. Sci. **68**, 314 (2013).
[44] C. Freysoldt, J. Neugebauer, and C. G. Van de Walle, Phys. Rev. Lett. **102**, 016402 (2009).
[45] Y. Kumagai and F. Oba, Phys. Rev. B **89**, 195205 (2014).
[46] Y. Kumagai, pydefect, https://github.com/kumagai-group/pydefect.
[47] T. Gake, Y. Kumagai, C. Freysoldt, and F. Oba, Phys. Rev. B **101**, 020102(R) (2020).
[48] W. Chen and A. Pasquarello, Phys. Rev. B **88**, 115104 (2013).
[49] T. Ishiguro, A. Kitazawa, N. Mizutani, and M. Kato, J. Solid State Chem. **40**, 170 (1981).
[50] B. Koehler and M. Jansen, Z. Anorg. Allg. Chem. **543**, 73 (1986).
[51] M. Shimode, M. Sasaki, and K. Mukaida, J. Solid State Chem. **151**, 16 (2000).
[52] Y. Hinuma, G. Pizzi, Y. Kumagai, F. Oba, and I. Tanaka, Comput. Mater. Sci. **128**, 140 (2017).
[53] C. W. Teplin, T. Kaydanova, D. L. Young, J. D. Perkins, D. S. Ginley, A. Ode, and D. W. Readey, Appl. Phys. Lett. **85**, 3789 (2004).
[54] J. P. Perdew, K. Burke, and M. Ernzerhof, Phys. Rev. Lett. **77**, 3865 (1996).
[55] V. I. Anisimov, J. Zaanen, and O. K. Andersen, Phys. Rev. B **44**, 943 (1991).
[56] J. B. Varley, A. Janotti, C. Franchini, and C. G. Van de Walle, Phys. Rev. B **85**, 081109(R) (2012).
[57] G. Miceli, W. Chen, I. Reshetnyak, and A. Pasquarello, Phys. Rev. B **97**, 121112(R) (2018).
[58] T. Gake, Y. Kumagai, and F. Oba, Phys. Rev. Mater. **3**, 044603 (2019).
[59] D. Cahen and A. Kahn, Adv. Mater. **15**, 271 (2003).
[60] Y. Kumagai, K. T. Butler, A. Walsh, and F. Oba, Phys. Rev. B **95**, 125309 (2017).
[61] Y. Hinuma, Y. Kumagai, I. Tanaka, and F. Oba, Phys. Rev. Mater. **2**, 124603 (2018).
[62] Y. Hinuma, T. Gake, and F. Oba, Phys. Rev. Mater. **3**, 084605 (2019).
[63] S. B. Zhang, S.-H. Wei, and A. Zunger, J. Appl. Phys. **83**, 3192 (1998).
[64] S. B. Zhang, S.-H. Wei, and A. Zunger, Phys. Rev. Lett. **84**, 1232 (2000).
[65] H. Hosono, Jpn. J. Appl. Phys. **52**, 090001 (2013).
[66] Y. Hinuma, Y. Kumagai, F. Oba, and I. Tanaka, Comput. Mater. Sci. **113**, 221 (2016).
[67] K. Momma and F. Izumi, J. Appl. Crystallogr. **44**, 1272 (2011).
[68] R. W. Nunes and X. Gonze, Phys. Rev. B **63**, 155107 (2001).
[69] S. Baroni and R. Resta, Phys. Rev. B **33**, 7017 (1986).
[70] S. L. Dudarev, G. A. Botton, S. Y. Savrasov, C. J. Humphreys, and A. P. Sutton, Phys. Rev. B **57**, 1505 (1998).